

On the decoupling and reaccrion of low density, line-driven winds

John M. Porter and Barry A. Skouza

Astrophysics Research Institute, Liverpool John Moores University, Twelve Quays House, Egerton Wharf, Birkenhead, L41 1LD, UK
(jmp@astro.livjm.ac.uk)

Received 7 August 1998 / Accepted 7 January 1999

Abstract. The flow generated by low-density radiatively driven winds which decouple their gas and radiation fields is discussed. In particular we concentrate on flow which is still bound to the star and can therefore reaccrion. The wind decelerates after decoupling and eventually stalls. A shell of gas is generated, and we find that this shell is unstable and contracts back to the star with periods of hours to days.

We find that the pulsating shells may be difficult to observe, as their emission is variable and the maximum emission at H_{α} (of $\sim 1\%$ of the continuum) occurs over a small fraction of the shell cycle.

Key words: hydrodynamics – stars: circumstellar matter – stars: early-type – stars: mass-loss

1. Introduction

The winds from hot stars are thought to be generated by radiation pressure on optically thick UV resonance lines, and the theory of line-driven flow is very successful in accounting many observed wind features (see Castor et al. 1975, Abbott 1980, Pauldrach et al. 1986, Kudritzki et al. 1989).

In low density winds, however, there exists the possibility that the radiation force and the wind flow may decouple (Springmann & Pauldrach 1992, Porter & Drew 1995 [hereafter PD95], Babel 1996). The decoupling process strips the metallic ions from the rest of the plasma, and as the radiative force on the flow is mediated by the ions, then the wind receives no further acceleration. The winds which are most likely to undergo this decoupling are B star winds (Babel 1996, PD95), and metallic A star winds (Babel 1995). The frictional interaction between the metallic ions and the rest of the wind may also seriously interfere with the radiative equilibrium (Springmann & Pauldrach 1992, Gayley & Owocki 1995). Decoupling radii for low density winds may be close to the photosphere for B stars (PD95) or indeed may be associated with the photosphere on the case of some A star winds (Babel 1995), where there is no region outside the photosphere where a fully coupled wind exists.

The line-driven wind accelerates normally when fully coupled to the radiation field, but once decoupled cannot receive any further acceleration. It is possible that the wind will decouple before it has reached escape velocity, in which case the decoupled flow will stall at some radius and fall back toward

the star. It is this aspect of decoupled flows which is examined in this paper.

The rest of this paper is structured as follows: in Sect. 2 the physics of wind decoupling is examined, and in Sect. 3 hydrodynamical simulations of decoupled winds are presented. The observational signatures of the shells are presented in Sect. 4 and a discussion and conclusions are given in Sect. 5.

2. Decoupling physics

There are two ways in which the radiation and matter fields in a line-driven wind may decouple: ion stripping (PD95, Springmann & Pauldrach 1992) and shock decoupling (PD95, Krolik & Raymond 1985).

The physics of ion stripping was first noted in the context of electrical conductivity by Dreicer (1959, 1960) and has its roots in the basic mechanism allowing optically thick metallic ion lines to mediate the force on a wind. The metallic ions are accelerated via photon scattering off their UV lines. The ions then share this acceleration with the rest of the wind (hydrogen and helium ions) by a process similar to friction. This frictional interaction depends on the relative drift velocity of the ions through the rest of the wind. For low drift velocities the force is proportional to the drift velocity, however it reaches a maximum when the drift and thermal kinetic energies are equal. Beyond this the frictional interaction decreases rapidly with increasing drift velocity. Therefore if the ions' drift velocity does become large enough, then as there is little or no frictional interaction with the rest of the wind, they may freely accelerate. This leaves the rest of the wind with no acceleration, and it will then just be acted upon by the gravitational attraction of the central star.

Shock decoupling occurs in a different way. It has been known that hot star winds may be unstable to the growth of instabilities for some time (Lucy & Solomon 1970, MacGregor et al. 1979, Owocki & Rybicki 1984) although it is unclear whether the winds are inherently unstable or only advectively unstable (see the review by Owocki 1991). If a low density wind passes through a strong shock, then the postshock gas may be too diffuse to cool radiatively, and so the gas remains in its high temperature, superionized state (Krolik & Raymond 1985). The wind may decouple from the radiation if the postshock gas remains out of equilibrium, as the main metallic species responsible for line-driving have been ionized away (Castor 1987).

Although both of these processes may in principle occur, only the former (ion stripping) is considered here as it is more deterministic – the decoupling radius for shock decoupling can only be calculated if the star’s X-ray emission (to determine the shock velocity) and mass-loss rate are available, whereas for ion stripping, only the mass-loss rate is required. It should be noted that the decoupling radius is similar in each case (see PD95).

For ion stripping, the decoupling radius r_d may be estimated by considering the relative velocity between the ions and the rest of the wind. As it is this drift velocity which sets the frictional interaction then it also defines how much acceleration is imparted to the rest of the wind. When the drift velocity becomes comparable to the ions thermal speed, the frictional interaction reaches a maximum beyond which it falls with increasing drift velocity. At this point the frictional interaction between the ions and the rest of the wind becomes small and the ions are (nearly) free to accelerate out of the wind. This radius is where the matter and radiation fields effectively decouple. For a beta-velocity law this yields

$$\frac{\beta v_{\infty 3}^3 (1 - R_*/r_d)^{3\beta-1} T_4 R_*}{\dot{M}_{-9}} = 1.5 \times 10^3 Y_i Z_i^2 \ln \Lambda, \quad (1)$$

(see Springmann & Pauldrach 1992 and also Gayley & Owocki 1995) where $v_{\infty 3}$ is the terminal velocity of the wind measured in units of 10^3 km s^{-1} , and the stellar radius R_* is expressed in solar units. Also Y_i is the mass fraction of the ions, Z_i is the degree of ionization, and $\dot{M}_{-9} \equiv \dot{M}/10^{-9} M_{\odot} \text{ yr}^{-1}$ is the mass loss rate derived from UV line profiles. T_4 is the temperature of the gas in units of 10^4 K and $\ln \Lambda$ is the Coulomb logarithm. The approach of calculating the ion-stripping radius used to derive Eq. 1 is, however, strictly only valid when the wind is fully coupled.

Therefore, a more exact calculation needs to be undertaken including the precise frictional force expression (e.g. see Springmann & Pauldrach 1992, Dreicer 1959, 1960). Although the frictional heating may increase the temperature of the wind and cause decoupling at smaller radii (PD95 noted this fact), the decoupling radii and velocities for a model B2 star have been calculated assuming isothermality. Temperature profiles of coupled radiatively-driven winds have been calculated by Drew (1989) using a full description of radiative heating and cooling processes in the wind. Drew’s calculations show that the wind temperature falls below $0.6T_{\text{eff}}$ only for $r > 2R_*$, although the frictional heating from the relative drift of ions through the rest of the wind was not included. Therefore the assumptions made here that the wind temperature is $0.8T_{\text{eff}}$ (Klein & Castor 1978), and that the flow is isothermal is probably not seriously in error.

For all the calculations undertaken in this paper, we use a “standard” B2V star which has stellar parameters of $M_* = 7.5M_{\odot}$, $R_* = 4.0R_{\odot}$, $T_{\text{eff}} = 20,000 \text{ K}$. The escape velocity of this star is $v_{\text{esc}} = 840 \text{ km s}^{-1}$, and the fully coupled terminal wind velocity is $v_{\infty} = 2.2\alpha v_{\text{esc}}/(1 - \alpha) = 2260 \text{ km s}^{-1}$ (Friend & Abbott 1986), for the line-driving parameter $\alpha = 0.55$ (see Castor et al. 1975). The decoupling radii and velocities

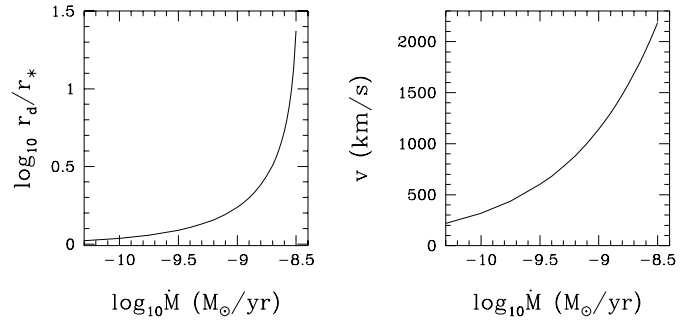


Fig. 1. Decoupling radii (left) and velocity (right) for a $7.5M_{\odot}$, $4.0R_{\odot}$, $2 \times 10^4 \text{ K}$ star as a function of mass-loss rate. The escape velocity is 840 km s^{-1} and the wind terminal velocity is 2260 km s^{-1} .

have been calculated for our standard star, and are presented as a function of mass-loss rate in Fig. 1.

The escape velocity of the star is 840 km s^{-1} and so from Fig. 1, it can be seen that if the mass-loss rate is less than $\sim 10^{-9.2} M_{\odot} \text{ yr}^{-1}$ ($= 6.3 \times 10^{-10} M_{\odot} \text{ yr}^{-1}$), then the wind will decouple and *still* be bound to the star.

3. Results

3.1. Analytic considerations

If the radiation and matter fields decouple at a velocity $v_d < v_{\text{esc}}$ then, as noted above, the material is still bound to the star. In this case the local radial velocity must be calculated for flow in a gravitational field. The radial velocity will decrease until the flow stalls at an outer radius r_s which can be estimated by equating the change in potential and kinetic energies, leading to

$$\frac{r_s}{R_*} \approx \left[\frac{R_*}{r_d} - \frac{1}{2} \left(\frac{R_* a^2}{GM_*} \right) \left(\frac{v_d}{a} \right)^2 \right]^{-1}. \quad (2)$$

As there is flow still with positive radial momentum behind this stalling front, a shell of stalled wind will form being supported by the ram pressure of the gas behind it. If we assume that the shell *can* be supported by the wind at some radius r_{shell} , then we can estimate the maximum total mass in the shell. The supporting ram-pressure P_{ram} of the stalling gas will be ρv^2 where ρ is the density and v is the local radial velocity. The oppositely directed pressure generated by the shell is due to the attractive gravitational force of the star $GM_* M_{\text{shell}}/r_{\text{shell}}^2$ where M_{shell} is the shell mass and G is the gravitational constant. This force acts over the surface area of the shell $4\pi r_{\text{shell}}^2$. Balancing the two oppositely directed pressures yields

$$M_{\text{shell}} \approx \frac{\dot{M} v r_{\text{shell}}^2}{GM_*}. \quad (3)$$

Here we have used the mass-continuity equation for spherical flows $\dot{M} = 4\pi r^2 \rho v$, where \dot{M} is the mass-loss rate of the wind. If $v_2 = v/100 \text{ km s}^{-1}$ and $\dot{M}_{-9} = \dot{M}/10^{-9} M_{\odot} \text{ yr}^{-1}$, then

$$\frac{M_{\text{shell}}}{M_{\odot}} \approx 1.2 \times 10^{-14} \dot{M}_{-9} v_2 \left(\frac{r_s}{R_{\odot}} \right)^2 \left(\frac{M_*}{M_{\odot}} \right)^{-1}. \quad (4)$$

Note that a distinction has been made between the stalling radius r_s and the radius of the shell r_{shell} . This is because the shell will only appear at the stalling radius if the wind first expands out into a vacuum. If there is any ambient density around the star ρ_{amb} , then this is swept up into the shell when the wind is “turned on”.

The evolution of the wind will broadly be composed of several parts. Initially the wind will be driven into the surrounding medium and will sweep up a shell of ambient gas. This shell will stop expanding when the shell and ram pressures balance. The shell then grows as it is receiving gas from the wind (at presumably the same rate as the mass-loss rate from the star). Finally the shell becomes too massive to be supported and will fall back toward the star.

If we assume that ρ_{amb} is small then the shell radius is the stalling radius. Also the wind’s ram pressure in this case is the thermal pressure ρa^2 , where a is the sound speed. For stalling radii of $r_s \approx 5R_* = 20R_\odot$ the shell mass for our standard star with a mass-loss rate of $10^{-9.5}M_\odot \text{ yr}^{-1}$ which will be supported by the stalling wind is $M_{\text{shell}} \sim 3 \times 10^{-14}M_\odot$. Given that the shell mass grows at a rate of \dot{M} , we find that it is stable for a time

$$t = 380v_2 \left(\frac{r_s}{R_\odot} \right)^2 \left(\frac{M_*}{M_\odot} \right)^{-1} \text{ s} \quad (5)$$

which for the example above is $t \approx 1\text{hr}$. The timescales here are similar to the flow timescale of the wind (approximately $R_*/v \approx 1\text{hr}$ for a wind speed of 1000 km s^{-1}).

After this time the shell’s mass will have increased such that there is insufficient ram pressure to levitate the shell and so it will fall back to the star. As the shell falls inward, the wind ram pressure increases - both the wind density and the radial velocity v increase (Mach numbers in radiatively driven flows can be ~ 100). However, the increasing mass of the shell is now acting over a smaller area. Hence the effective pressure exerted by the shell inward due to the gravitational attraction by the central star increases. This pressure of the shell is the gravitational force divided by the area of the shell: $P_{\text{shell}} \propto r^{-4}$ whereas the ram pressure is $P_{\text{ram}} \propto v/r^2$. The ratio of these two pressures is

$$\frac{P_{\text{shell}}}{P_{\text{ram}}} = \frac{8.6 \times 10^{-12}}{\dot{M}_{-9}v_2} \left(\frac{M_*}{M_\odot} \right) \left(\frac{M_{\text{shell}}}{M_\odot} \right) \left(\frac{r}{R_\odot} \right)^{-2}. \quad (6)$$

Note that in the decoupled part of the wind $v \sim r^{-1/2}$, and so as M_{shell} increases and moves toward the star (r decreases) the ratio above grows. This then implies that the shell can not be stable (balanced) at any radius, and must fall back to the star.

Once the shell has contracted to the star, the wind is free again to expand to its stalling point and the cycle restarts. This analysis predicts that stars with bound decoupled winds will inevitably produce periodic structures associated with the wind. However, a word of caution is warranted here: this scenario predicts that a shell of gas should form and collapse onto the star with timescales of hours–days. There is a possibility that the oppositely directed gravity and pressure gradients as the shell contracts may break up the shell due to Rayleigh-Taylor instabilities.

3.2. Numerical hydrodynamic modelling

To illustrate the preceding section’s scenario, a 1D numerical hydrodynamic simulation has been completed. The computer code utilises the second order Godunov scheme due to Falle (1991) to solve the hydrodynamic equations. The line force is calculated using the standard Castor et al. (1975) formalism of the force multiplier, supplemented with the finite-disc correction (Friend & Abbott 1986) and the density weighting factor from Abbott (1982). The grid has a spacing of $0.005R_*$ at $r = R_*$, increasing by 1.5% to a maximum spacing of $0.09R_*$ at the outer radius of $6.75R_*$ (there are 200 grid points). The outer boundary allows gas to flow through it freely, whereas the inner boundary has the density fixed at $10^{-12} \text{ g cm}^{-3}$, and the velocity extrapolated from the neighbouring zones. We can expect that after a time the radial velocity at the outer boundary will become negative and matter will flow into the computational domain. This causes the density to rise at the outer parts of the simulation, and finally lead to a significant ram pressure acting on the shell from infalling material. Ultimately this leads to the central star being surrounded by high density, infalling material, completely thwarting even the initiation of the wind! Clearly this is an artifact of the outer boundary. After experimentation, it is found that the outer boundary which illustrates the scenario most effectively is a “valve”, i.e. the boundary is free-flow when the radial velocity is greater than zero, but otherwise we set the radial velocity to zero, and the density to a small value ($10^{-30} \text{ g cm}^{-3}$).

In order to examine the effect of differing mass-loss rates on the flow we prepared five fully-coupled wind solutions as initial conditions. These have been generated for our standard B2 star. We find that the mass-loss rate for this star is $\sim 10^{-8.3}M_\odot \text{ yr}^{-1}$. As we require differing (and much lower) mass-loss rates to assess its effect on the decoupled flows, we have reduced the radiation force by as much as an order of magnitude. This may be seen as a change in metallicity – the radiative acceleration is proportional to the metallicity raised to the power of $1 - \alpha$ (Abbott 1982, Castor et al. 1975). The lowest metallicity model implied is then 0.006 solar. By reducing the line force we have generated simulations with have mass-loss rates in the range $(1.6\text{--}4.4) \times 10^{-10}M_\odot \text{ yr}^{-1}$ (see Table 1). We have fitted a “beta” velocity law to the first 50 points (upto $1.3R_*$) of the initial conditions and find that they are all well fit by $v = 2100(1 - R_*/r)^{0.8} \text{ km s}^{-1}$, although for the models with higher mass loss rate, β falls to 0.73. With this velocity structure, we calculate the decoupling velocities and radii as described in Sect. 2. These are presented in Table 1. Note, we have assumed that all models have solar metallicity for the calculation of the decoupling radii, which may be inconsistent with the generation of the initial conditions if the low radiative acceleration is interpreted as due to a change in metallicity.

In order to simulate the decoupled flow, we use these fully coupled wind structures as initial conditions and simply turn off the radiation force at the decoupling radius. The flow is calculated in each simulation for at least ten shell episodes to

Table 1. Model parameters for the simulations. r_d and v_d are the decoupling radius and velocity respectively. The stalling radius r_s is calculated from Eq. 2. The shell period and the median maximum emission measure (over several cycles) are listed in Columns 6 and 7.

Model	$\log_{10}\dot{M}$ ($M_{\odot}\text{ yr}^{-1}$)	$r_d(R_*)$	v_d (km s^{-1})	$r_s(R_*)$	$\log_{10}\text{EM}$	period (hr)
A	-9.35	1.27	590	3.50	56.0	27.8
B	-9.46	1.26	568	3.09	55.7	20.8
C	-9.59	1.23	522	2.39	55.1	14.6
D	-9.68	1.20	447	1.82	54.6	8.9
E	-9.78	1.17	378	1.53	54.1	6.6

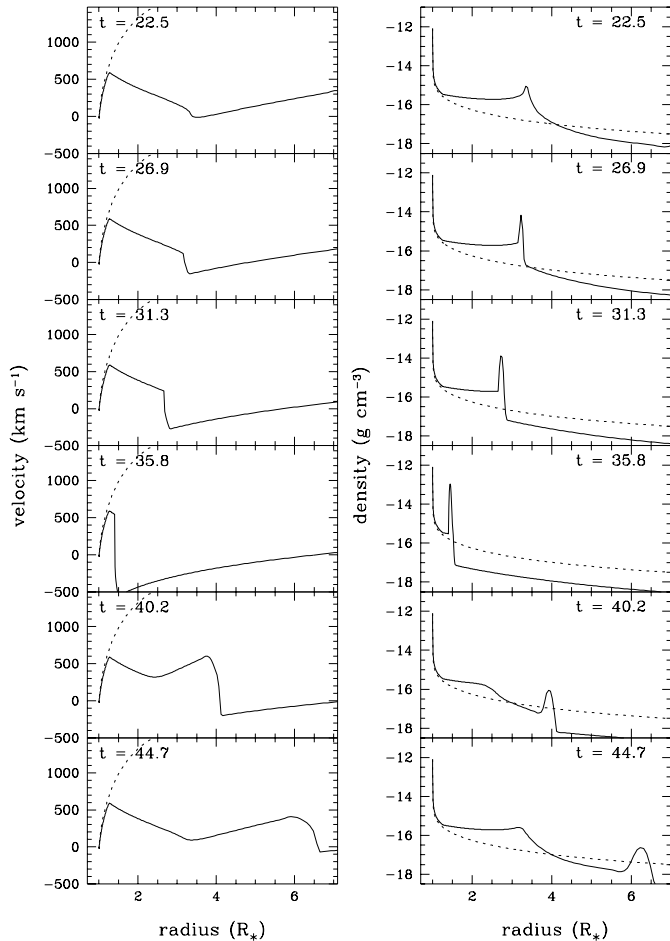


Fig. 2. Numerical hydrodynamic modelling of a the formation and evolution of a spherical shell (Model E). The dotted line is the steady, fully-coupled starting condition. The plots are labelled in time (in hours). The radiation force was set to zero at radii larger than $1.27R_*$.

ensure that the initial conditions have no effect on the subsequent flow.

Part of the simulation's results for model A are shown in Fig. 2 – the panels of velocity (left) and density (right) are labelled with the time in hours (the starting point for the time has been shifted to coincide with Fig. 3). All the models have qualitatively the same behaviour with only the physical scales changing from model to model. The first couple of cycles have not been shown to remove any start-up transients. The dotted lines on the panels are the starting condition described above as a ref-

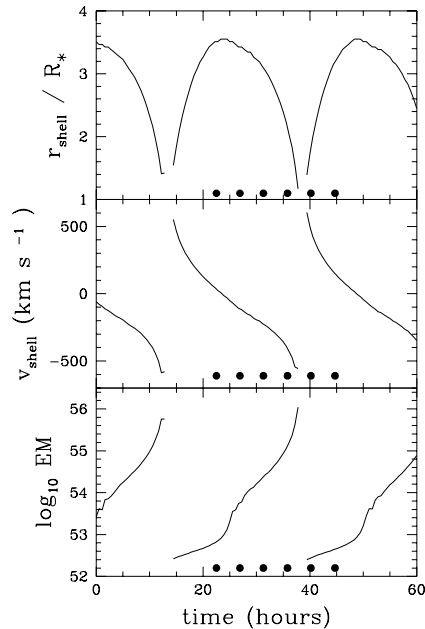


Fig. 3. Time resolved attributes of the shell for Model A. Position (*top*) and velocity (*middle*) of the shell in time through a shell episode. The *lower panel* shows the total emission measure of the wind structure. The solid dots indicate the times of the corresponding panels in Fig. 2.

erence. The first panel shows the dense shell forming at a radius of $3.5R_*$. The shell's mass increases (to $\sim 1.8 \times 10^{-13} M_{\odot}$) until its weight is large enough to overcome the wind ram-pressure, and so it contracts toward the star (at around 5hrs later – the second panel of Fig. 2). The shell gains mass and falls faster with time (panels 3 and 4), finally collapsing onto the star just before 37hrs. Once the shell makes contact with the star, the wind is again free to accelerate to decoupling. This process sweeps up some of the material left behind by the previous cycle's contracting shell and a new shell is generated moving outwards (the lower two panels of Fig. 2). The whole cycle takes around 28hrs. Although the timescale for the shell growth is very similar to our previous estimate, the timescale for the whole cycle is ~ 1 day for this star. The periods for the shell episodes for the different models are shown in Column 7 of Table 1.

We have calculated the emission measure $\text{EM} = \int n_e^2 dV$ (where n_e is the electron density, and V is the volume of the shell) for the simulations. The median maximum value for the emission measure from all the simulated cycles is shown in

Column 6. Fig. 3 shows how the radius, velocity, and emission measure changes with time through a shell episode. We have identified the shell at the point where there is a local maximum in density (when the shell is close to the star it becomes difficult to identify unambiguously and so these points have been left out of Fig. 3). The wind initially sweeps up the ambient gas creating a low density-contrast shell. In this phase the shell is decelerating from the decoupling radius, and moving out in radius. Finally the shell comes to rest ($v_s = 0$ at $r \approx 3.5R_*$), and it starts to gain mass. The emission measure starts to increase significantly during this time. When it cannot be supported any longer the shell starts to fall back toward the star, finally coming into contact with the star at a velocity of around -500 km s^{-1} .

All of the simulations produce very similar plots except the scaling in time and position are different. We find that the stalling radii are very similar to those predicted using Eq. 2 (Table 1, Column 3).

The period for initial shell growth has already been shown to be dependent on the mass-loss rate via the stalling radius (Eq. 5) which is, in turn, set by the decoupling radius. As the mass-loss rate increases, the decoupling velocity/radius increases (see Table 1), and so the stagnation radius (at which the shell forms) also increases. We expect that the scaling relationships in the shell-growth timescale (Eq. 5) is similar for the timescale of the shell episode as a whole, although the time for shell growth is only a fraction of the shell cycle. Hence we expect that the period should be proportional to the stalling radius squared. In Fig. 4 the logarithmic period-stalling radius relationship is displayed. We have performed a least-squares fit to the above data and find that the period P is related to the stalling radius via $P = 3.22r_s^{1.7}$ which is close to the expected scaling. We also find that the maximum emission measure follows the same scaling with radius.

4. Observable signatures

The total mass in the shell will typically be the wind mass-loss rate multiplied by the total lifetime of the shell. Timescales of \sim day have been found from the previous section, yielding maximum shell masses of $M_{\text{shell}} \sim 10^{-13} - 10^{-12} M_\odot$. Clearly such a low mass will not have a large influence on the gross observational properties of the star. The most obvious effect of decoupling is that the maximum wind velocity will be observed to be lower than the terminal velocities from theoretical studies – a phenomenon which has been known observationally for some time (Grady et al. 1987).

Would the shell give rise to any variation in the lines of the star? Clearly there would be no change in the UV line profiles until the shell radius becomes less than the decoupling radius. Here the maximum edge velocity will decrease as the shell falls toward the star. However, the occurs only over a small fraction of the time of the whole cycle.

It may be possible that the shell may provide a varying component to the hydrogen lines. Let us assume that the shell is always optically thin and calculate the excess emission at H_α . This is simply $j = h\nu\alpha_{H_\alpha}^{\text{eff}} n_e n_p / 4\pi \text{ erg cm}^{-3} \text{ s}^{-1} \text{ st}^{-1}$ where

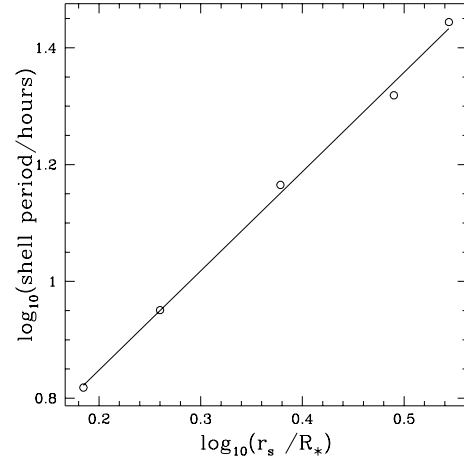


Fig. 4. The log-log relationship between the period of shell episodes P and the stalling radius of the wind r_s from Eq. 2. The straight line is the least-squares fit to the points: $P = 3.22(r_s/R_*)^{1.7}$ hours.

n_e and n_p are the electron and proton number densities, and $\alpha_{H_\alpha}^{\text{eff}}$ is the H_α recombination coefficient of $5.96 \times 10^{-14} \text{ cm}^3 \text{ s}^{-1}$ assuming Case B recombination at 20,000 K (Osterbrock, 1989). Assuming that the emission is optically thin then the shell produces a flat-topped emission profile with a range in wavelength given by the velocity of the shell. When the shell is close to the star, then the star occults the far side of the shell and so curtails the maximum blueshifted emission. If the angle between the pole and a point on the shell is θ , then emission from that point is Doppler shifted by

$$\delta\lambda = \lambda \frac{v_s}{c} \sin\theta \quad (7)$$

where v_s is the velocity of the shell, and c is the speed of light. Combining this with the expression for j , and integrating the volume emitting at the same wavelength, we derive the emission as

$$j = \frac{h\alpha_{H_\alpha}^{\text{eff}} n_e n_p}{2} r_s^2 dr \left(\frac{c}{v_s} \right) \text{ erg s}^{-1} \text{ st}^{-1} \text{ Hz}^{-1} \quad (8)$$

We assume that that star is emitting as a black-body and calculate the fraction of the black body flux the shell emits (of course in a *real* star there is also photospheric absorption). After some simple manipulation we find that this ratio is

$$\mathcal{R} = \frac{(e^{h\nu/kT} - 1)}{4} \frac{c^3 \alpha_{H_\alpha}^{\text{eff}} EM}{\nu^3 4\pi R_*^2 v_s} \quad (9)$$

where the symbols have their usual meanings. This extra component extends over a wavelength range

$$\lambda_0 \left(1 - \frac{v_s}{c} \sqrt{1 - \left(\frac{R_*}{r_s} \right)^2} \right) < \lambda < \lambda_0 \left(1 + \frac{v_s}{c} \right) \quad (10)$$

where $\lambda_0 = 6563 \text{ \AA}$ is the central wavelength of the line.

We have calculated the extra component of H_α for Model A and present it as a time series in Fig. 5. The grey scale is linear with a range of 0–1% of the continuum with the the darkest tone

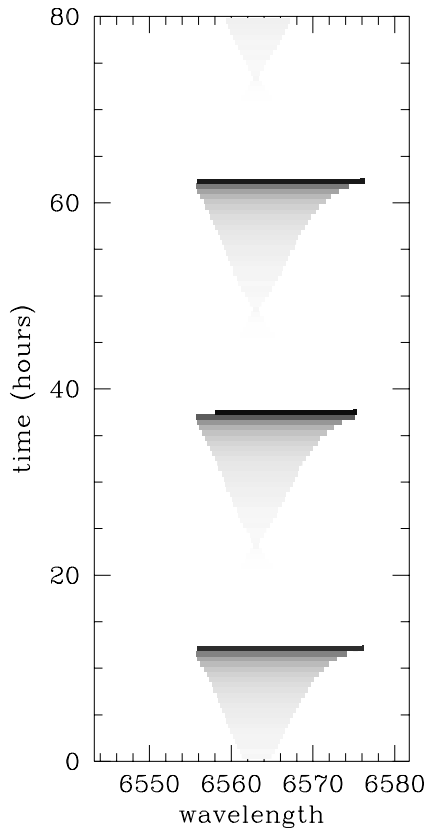


Fig. 5. Grey-scale representation of the time series of the excess line emission at H_{α} due to the shell for Model A (see text). The grey scale is linear, and the darkest tones correspond to 1% of the continuum emission.

corresponding to 1%. We find that the maximum value of \mathcal{R} for Model A is $\sim 1\%$, i.e. the flat-topped shell component has a contrast of $\sim 1\%$ of the continuum flux. Whilst this is clearly an observable amount, it is only present at significant values for a small of the cycle.

5. Discussion and conclusions

We have demonstrated that low density radiation-driven flows may decouple before the wind becomes unbound from the star, and therefore will reaccrete. Abbott & Friend (1989) discussed a model of a line-driven wind with a line force cut-off to mimic the effects of shocks in the wind. However, their models had force cut-offs such that the wind beyond decoupling was unbound and therefore would escape from the star.

This is the first suggestion that these flows may still be bound to the star post-decoupling. We have examined the attributes of the periodic shell structures formed in the flow and have calculated the line emission.

From our analysis we conclude that these shells may be observable in a line monitoring campaign, with the largest emission coming from stars with winds which decouple close to the escape velocity. These stars will also have the longest period for the shells making it more probable that the shell can be observed.

It is worthy of note that this process of reaccretion will change the metallicity in the outer layers of the star over a long time period. As it is only the metals which become unbound, then their abundance decreases with time in the outer layers when the shells reaccrete. In a future study we will address the case of rotating winds which may be applicable to classical Be stars as these stars do seem to have small mass-loss rates.

Acknowledgements. JMP is supported by a PPARC postdoctoral research assistantship. The referee, Dr. S.P. Owocki is thanked for constructive suggestions which improved this paper.

References

- Abbott D.C. 1980, ApJ 242, 1183
 Abbott D.C. 1982, ApJ 259, 282
 Abbott M.J., Friend D.B., 1989, ApJ 345, 505
 Babel J., 1995, A&A 301, 823
 Babel J., 1996, A&A 309, 867
 Castor J.I., Abbott D.C., Klein R.I., 1975, ApJ 195, 157
 Castor J.I., 1987, In: Lamers H.J.G.L.M., de Loore C.W.H. (eds.) *Instabilities in Luminous Early-Type Stars*. D. Reidel, The Netherlands, p. 159
 Dreicer H., 1959, Phys. Rev. 115, 238
 Dreicer H., 1960, Phys. Rev. 117, 329
 Drew J.E., 1989, ApJS 71, 267
 Falle S.A.E.G., 1991, MNRAS 250, 581
 Friend D.B., Abbott D.C., 1986, ApJ 311, 701
 Gayley K.G., Owocki S.P., 1995, ApJ 446, 801
 Grady C.A., Bjorkman K.S., Snow T.P., 1987, ApJ 320, 376
 Klein R.I., Castor J.I., 1978, ApJ 220.902
 Krolik J.H., Raymond J.C., 1985, ApJ 298, 660
 Kudritzki R.P., Pauldrach A., Puls J., Abbott D.C., 1989, A&A 219, 205
 Lucy L.B., Solomon P.M., 1970, ApJ 159, 879
 MacGregor K.B., Hartmann L., Raymond J.C., 1979, ApJ 231, 514
 Osterbrock D.E., 1989, *Astrophysics of Gaseous Nebulae and Active Galactic Nuclei*. Oxford University Press
 Owocki S.P., 1991, In: Hubeny I., Crivellari L. (eds.) *Stellar Atmospheres: Beyond Classical Models*. Kluwer, Dordrecht, p. 337
 Owocki S.P., Rybicki G.B., 1984, ApJ 284, 337
 Pauldrach, A., Puls, J., Kudritzki, R.P. 1986, A&A 164, 86
 Porter J.M. Drew J.E., 1995, A&A 296, 761 [PD95]
 Springmann U.W.E., Pauldrach A.W.A., 1992, A&A 262, 515